Nanoscale

PAPER

View Article Online
View Journal | View Issue

Cite this: *Nanoscale*, 2014, **6**, 6860

Synthesis and electrochemical properties of silicon nanosheets by DC arc discharge for lithium-ion batteries†

Xiuhong Yu,[a] Fanghong Xue,*[a] Hao Huang,[a] Chunjing Liu,[a] Jieyi Yu,[a] Yuejun Sun,[a] Xinglong Dong,*[a] Guozhong Cao[ab] and Youngguan Jung[c]

Received 3rd December 2013
Accepted 15th March 2014

DOI: 10.1039/c3nr06418b

www.rsc.org/nanoscale

Two-dimensional (2D) ultrathin silicon nanosheets (Si NSs) were synthesized by DC arc discharge method and investigated as anode material for Li-ion batteries. The 2D ultrathin characteristics of Si NSs is confirmed by means of transmission electron microscopy (TEM) and atomic force microscopy (AFM). The average size of Si NSs is about 20 nm, with thickness less than 2.5 nm. The characteristic Raman peak of Si NSs is found to have an appreciable (20 nm) shift to low frequency, presumably due to the size effect. The synergistic effects of Ar^+ and H^+ lead to 2D growth of Si NSs under high temperature and energy. Electrochemical analyses reveal that Si NSs anode possesses stable cycling performance and fast diffusion of Li-ions with insertion/extraction processes. Such Si NSs might be a promising candidate for anode of Li-ion batteries.

Introduction

Si is the second most abundant element on earth and becomes the main material in modern electrical industry since the invention of the transistor in 1950s, which has been developing rapidly in electronic and photologic devices.[1] During the past decade, Si nanoarchitectures such as nanoparticles, nanotubes, nanowires, nanosheets, nanoporous materials and thin films have shown many promising potential applications due to large specific surface area, size-confinement effect, photoluminescence and unique electrochemical properties, *etc.*[2–8] They are also potential anode materials for Li-ion batteries with a high theoretical lithium storage capacity of 4200 mA h g^{-1} (ten times higher than 372 mA h g^{-1} for traditional carbonaceous materials) and a relatively low working potential.[9] However, Si anodes suffer from poor cycling stability, resulting from a severe volume change during insertion/extraction of lithium along with inherent low conductivity.[10] Much effort has been made to seek new strategies to overcome such challenges, including introducing second phase components,[11–13] nanostructure,[14–16] *etc.*

2D Nanomaterials, with an exceptionally high specific surface area, may show unique properties as compared to 0D or 1D nanomaterials. It is expected that thin 2D nanostructures exhibit advantages to stand volume change during the insertion/extraction process, and can apply more active sites to allow for effective use of limited spaces, as well as contribute to high energy density.[17] For example, graphene, one-atom thick 2D carbon material, has been reported with a theoretical lithium storage capacity of 744 mA h g^{-1} due to the formation of LiC_3 on both sides of graphene sheets, and the experimental results by Wang *et al.* showed a stable specific capacity of about 460 mA h g^{-1} after 100 cycles.[18] Kulish's calculation showed that Si NSs can be a potential anode material for Li-ion batteries.[19] Nevertheless, most literature sources on Si-anode Li-ion batteries are concentrated on 0D and 1D nanostructures. So far, there are very limited investigations on 2D Si-based nanomaterials reported in open literature.[20,21] For example, single-crystal Si monolayer sheets, so called silicene, has been successfully fabricated through chemical exfoliation from calcium disilicide ($CaSi_2$).[22] Kim *et al.* used a chemical vapor deposition process to synthesize free-standing single crystalline Si NSs with a thickness less than 2 nm.[23] Recently, Yan's group used graphene oxide (GO) NSs as sacrificial templates to synthesize ultrathin Si NSs, which exhibited lithium storage properties better than Si nanoparticles.[24] However, such fabrication processes are sophisticated and have a very low yield.

This paper reports on the synthesis of 2D Si NSs with a simple method, DC arc discharge under an atmosphere of argon and hydrogen. As a traditional technique, this method is well known for high yield, high purity of nanopowder products and ease of fabrication particular kinds of nanostructures. The structures, morphologies and electrochemical lithium storage properties of such Si NSs were characterized and investigated.

[a]*School of Materials Science and Engineering, Dalian University of Technology, Dalian 116023, P.R.China. E-mail: fhxue@dlut.edu.cn; dongxl@dlut.edu.cn*

[b]*Department of Materials Science and Engineering, University of Washington, Seattle, WA 98195, USA*

[c]*Department of Mechanical Engineering, Kumoh National Institute of Technology, Daehakro 53, Gumi, Gyeong-Buk, 730-701, Republic of Korea*

† Electronic supplementary information (ESI) available. See DOI: 10.1039/c3nr06418b

Results and discussion

The XRD pattern of the as-prepared Si NSs is shown in Fig. 1. The material exhibits a crystalline (c-Si) phase with a face-centered cubic (FCC) crystal system (JCPDS cards, no. 26-1481). According to the Scherer equation:

$$D_c = 0.89\lambda/(B\cos\theta) \quad (1)$$

where D_c is the size of the crystalline; B, the width at half height (FWHM) of the sample; θ, the diffraction angle; λ, X-ray wavelength. The calculated average crystallite size of Si NSs is about 22 nm. The XRD pattern of raw Si bulk material is shown in Fig. S2.† In a comparison of two XRD patterns, it is found that positions, widths and intensities of the diffraction peaks are greatly altered, indicating the lattice constant, grain size and preferred growth were changed and occurred in the Si NSs.

The structures and morphologies of Si NSs were characterized by TEM and a typical image is shown in Fig. 2a. Si NSs have a rather uniform size distribution and very similar morphology. They all seem to have irregular curved edges and corners, with similar thickness judging from a very similar transparency under TEM observation. The sizes of most Si NSs are about 20 nm, which is in accordance with the XRD results. Fig. 2b is the selected area electron diffraction (SAED) pattern of Si NSs. The diffraction dots and rings corresponding to (111), (220), (311) planes of Si reveal the crystalline state of Si NSs.

Fig. 3 shows an AFM image (left) of the as-prepared Si NSs in contact mode and the relevant height profile (right) labeled with arrows. In preparation of the AFM sample, the Si NSs had a strong tendency to gather together because of the surface tension as they were extracted from the solution. This tendency makes Si NSs look larger than those of the TEM result. Such Si NSs have a thickness of about 2.4 nm. It is clear that the NSs are only a few atomic layers thick. The ultrathin feature of the Si NSs leads to failure of acquiring clear lattice fringes in the high resolution transmission electron microscopic (HRTEM) images, as shown in Fig. S6a.†

The Si NSs powder was further characterized by Raman spectroscopy and the result is shown in Fig. 4. As we all know,

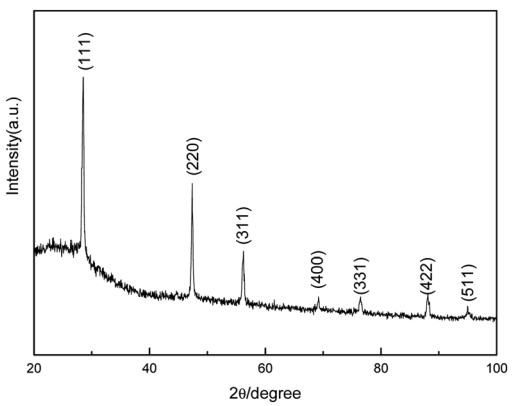

Fig. 1 XRD pattern of Si NSs fabricated by DC arc discharge method under an atmosphere of hydrogen and argon.

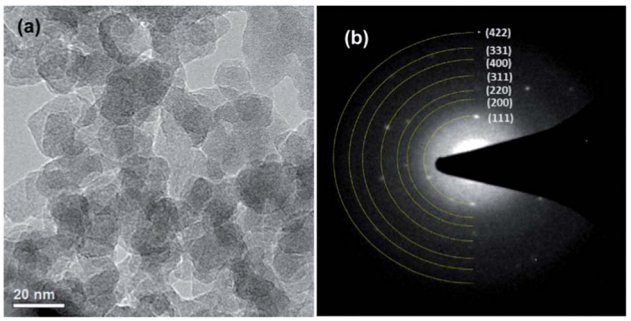

Fig. 2 (a) Typical low-magnitude TEM image of Si NSs, showing plate-shaped morphology. (b) The relevant SAED image of Si NSs.

Raman spectroscopy is a powerful technique used for specific check of the phonon modifications, induced in nanocrystals by quantum size effects.[25] The position, shape of the Raman peak, and its FWHM are sensitive to the size in the domains. It was reported that the Raman spectrum of crystal Si consisted of one sharp peak at 520 cm^{-1} originating from the microcrystalline.[26] It can be seen from Fig. 4 that the Raman spectrum of Si NSs has an intense peak at ~500 cm^{-1}, a visible shift (20 cm^{-1}) to lower frequency, with broadened FWHM. It has been verified in theory calculations and experimental works that the first order peak of Si nanocrystals shifts to a lower frequency with broadened FWHM due to the diameters' decrease.[27,28] Wang reported the first order Raman peak of Si nanowires shifts to 505 cm^{-1} when the diameter decreased to 10 nm.[29] For the present Si NSs, such Raman peak shift and broadening of FWHM are considered from the phonon confinement in the two-dimensional nanoscale Si crystal.[24] The Raman shift of 20 cm^{-1} from 520 cm^{-1} to 500 cm^{-1} further indicates just a few atomic layers of our sample. In addition, two broad peaks centered at 288 and 914 cm^{-1} can be assigned to the overtones of TA (X) and TO (L), respectively, which result from the relaxation of momentum conservation rules when the crystallite is reduced to nanoscale dimensions.[29]

Based on the above results, the plate-like characters of Si NSs are well confirmed. To our knowledge, this is the first report on the Si NSs fabricated by an arc discharge method. In order to understand the exceptive formation mechanism for such Si NSs in an atmospheric mixture of hydrogen and inert gas, the preparation atmospheres of a series of contrast experiments and the final morphologies, yields of the Si nanopowder

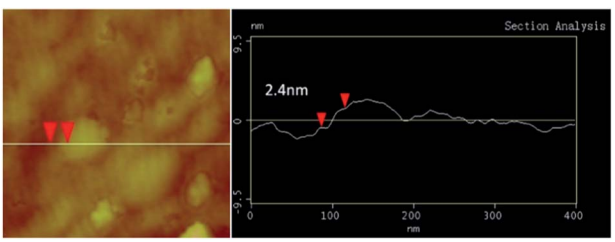

Fig. 3 AFM image of Si NSs (left) and section line analysis (right) as indicated, showing the ultrathin nature of Si NSs.

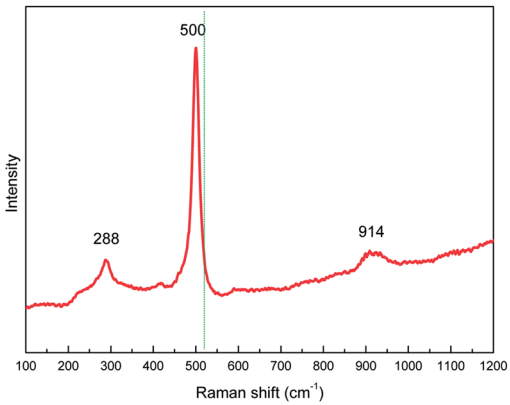

Fig. 4 Raman spectrum of the Si NSs, a peak shift of 20 cm^{-1} from 520 to 500 cm^{-1}.

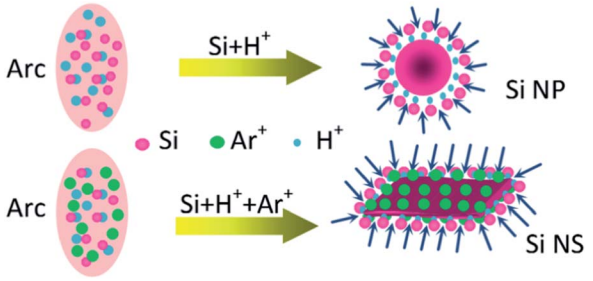

Fig. 5 Schematic formation mechanism for Si nanosheet (NS) and Si spherical nanoparticle (NP), by DC arc discharge method under atmospheres of hydrogen and hydrogen/argon, respectively.

products are summarized in Table 1. The relevant TEM and HRTEM images are shown in Fig. S4–S6.† The products of Si NSs have a higher yield than that of nanoparticles and nanoribbons in the given conditions. In an arc discharge process, hydrogen is a necessary component in serving as a source of hydrogen plasma with high energy and the inert gas usually has an effect of condensation. Hydrogen is easily ionized into H^+ ions at high temperature, and can promote the evaporation of bulk Si into atomic states. As shown in Fig. 5 (upper), the evaporated Si atoms nucleate and grow into a spherical nanoparticle (as shown in Fig. S5†) under the sole effect of H^+ ions, namely, H^+ ions favor an isotropic growth of Si nanoparticle. Nevertheless, under the synergistic effect of H^+ and Ar^+, the morphologies of Si products become sheet or ribbon-like shapes. Those were the results from a preferential growth along one or two dimensions, as seen in Fig. 5 (below) and Table 1. It is suggested that H^+ ions would equally affect the growth of Si cluster in all directions by a weak bond of Si and H, whereas Ar^+ ions collide with Si atoms to exchange energy and minimize the system energy, resulting in a selective influence on the growth of Si products according to its crystal planes. The collisions between high energy Ar^+ ions and Si atoms would restrict its incorporation (growth) on a higher energy crystal face. For example, because the (111) plane has the lowest surface energy, the growth rate in ⟨111⟩ direction was suppressed and then this crystal plane was exposed in final Si NSs.[30] Such consideration is well in agreement with the XRD result.

In order to investigate the electrochemical lithium storage properties of the Si NSs serving as anode, CR2025-type half-coin cells were adopted. In this work, we use the arc-discharge prepared graphene powders as conductive agent.[31] Mixed with 10 wt% of such kind of graphene in the electrode, our preliminary investigation indicated that the capacity of Si NSs anode was rapidly fading to 10 mA h g^{-1} from 300 mA h g^{-1} of the first discharge capacity. It was considered that such fast decline and the limited first capacity were attributable to an insufficiently electrical contact inside the Si NSs anode and the electrode should further be improved by increasing the content of conductive agent. It was also reported by Tarascon *et al.* that the Si-based battery showed best cyclability with 33.3 wt% of the carbon black conductive additives.[32] In this experiment, the weight ratio of 45 : 45 : 10 (Si NSs : conductive agent : binder) was set and a series of electrochemical measurements was carried out.

The initial three charge/discharge voltage profiles of the Si NSs anode are shown in Fig. 6a. In the first cycle, the discharge and charge capacities are 2553 and 1242 mA h g^{-1}, respectively, with an initial Coulombic efficiency of 49%. The large irreversible capacity can be mainly ascribed to the reductive decomposition of the electrolyte solution and the subsequent formation of the solid electrolyte interface (SEI) film on the anode surface, especially the large surface of Si NSs exposed to electrolyte would bring more irreversible capacity for the formation of SEI film, and also a portion to the irreversible insertion of lithium into Si matrix.[33] During the following two cycles, irreversible capacities decrease a lot. In the second cycle, the electrode delivers a discharge capacity of 1208 mA h g^{-1} and a Coulombic efficiency of 89%. The Coulombic efficiency further increases to 91% with a reversible capacity of 1020 mA h g^{-1} in the third cycle. From these curves, it can be seen that during the lithium insertion process the voltage drops quickly to 0.2 V, and then there is a flat discharge plateau, indicating the lithium inserted into Si matrix mainly occurs below 0.2 V.

Table 1 Morphologies and yields of Si nano-products obtained in atmospheres with different ratios of hydrogen and argon

Amount of hydrogen (MPa)	Amount of argon (MPa)	Morphology of the products	Yield (g h^{-1})
0.03	0	Nanoparticles (Fig. S4)	3.1
0.01	0.02	Nanosheets (Fig. 2)	8.4
0.01	0.05	Nanoribbons (Fig. S3)	0.04
0	0.03	No products	0

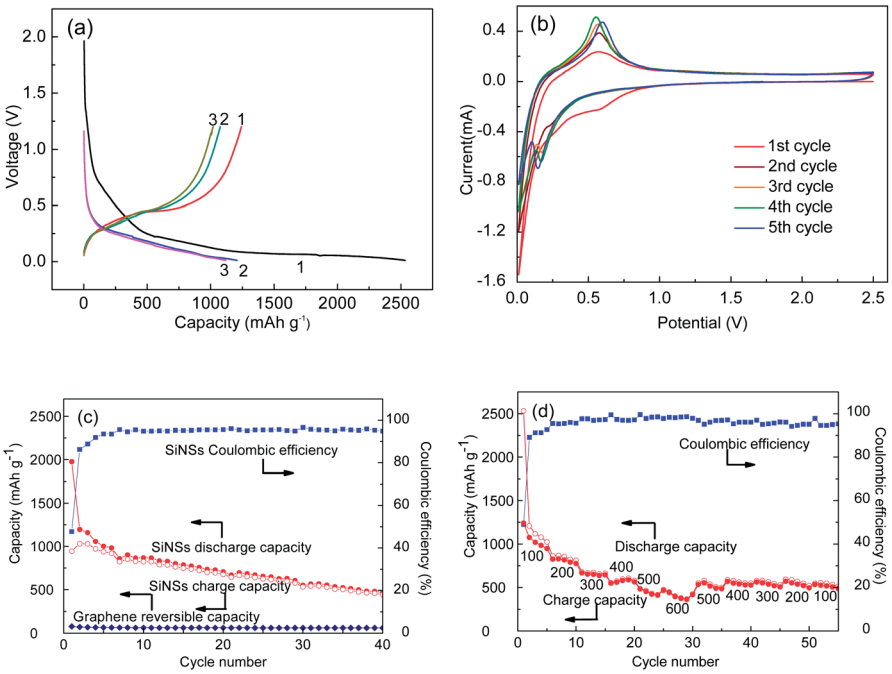

Fig. 6 (a) The initial three charge/discharge curves for the Si NSs anode at a current density of 100 mA g^{-1} between 0.01 and 1.2 V. (b) Cyclic voltammograms for the Si NSs anode from 0.01 to 2.5 V at a scan rate of 0.1 mV s^{-1}. (c) Cycling performance of the anode at a constant current density of 100 mA g^{-1} between 0.01 and 1.2 V and reversible capacity for graphene in the same conditions. (d) Cycling performance of the electrode at different current densities from 100 to 600 mA g^{-1} with an interval of 100 mA g^{-1} between 0.01 and 1.2 V.

Fig. 6b shows the CV curves of the initial five cycles. During the first cathodic scanning, a broad cathodic peak at 0.58 V is observed and disappeared in the following cycles, which resulted from the formation of SEI film on the electrode surface. In addition, one broad peak in the range of 0.2 to 0.01 V can be seen during the first discharge process, which corresponds to the lithium insertion process and the phase transition of amorphous lithium-rich Li_xSi phases to crystalline $Li_{15}Si_4$.[34] Upon the second cathodic scanning, a new peak can be observed at 0.23 V, which results from the high voltage lithium insertion into amorphous Si–Li phase and this process experiences an activation process.[35] During the first charge process, a strong peak at 0.58 V can be observed which is due to the extraction of lithium from Si–Li alloys. During the following cycles, this peak magnifies, indicating the improved extraction kinetics of lithium.[35] The transition processes can be described as follows:[36]

$$\mathrm{Si(crystal)} \rightarrow \mathrm{Li}_x\mathrm{Si(amorphous)} \rightarrow \mathrm{Li}_{15}\mathrm{Si}_4\mathrm{(crystal)} \leftrightarrow \mathrm{Si(amorphous)} \quad (2)$$

It can be seen from the CV results that there are no peaks relating to the lithium reacting with graphene and the cycling performance of graphene in Fig. 6c also shows the reversible capacity of graphene is only 60 mA h g^{-1} which can be ignored. So, graphene only acts as the conductive agent.

Fig. 6c shows the cycling performance of the Si NSs anode. It can be seen that the Coulombic efficiencies are always kept above 94% except the initial few cycles, indicating excellent reversible lithium storage properties. After 40 cycles, the charge capacity is 441.7 mA h g^{-1}, which is also higher than traditional carbonaceous materials. The Si NSs anode also shows good capacity retention at increased current density from 100 to 600 mA g^{-1} with an interval of 100 mA g^{-1} as shown in Fig. 6d. As the current density increased, though the charge capacities decrease to some extent, a capacity of 534 mA h g^{-1} can be recovered once the current density is restored to the initial 100 mA g^{-1}. This phenomenon indicates the good reversibility of Si NSs anode. The stable cycling performance of Si NSs anode can be due to the unique structure of Si NSs, which may effectively buffer the strain generated during the lithium intercalation process and also shorten the lithium ions transport distance.

To further understand the electrochemical performances, EIS was adopted to discuss the conductive and diffusive behavior of Si NSs anode. The Nyquist plots of Si NSs anode before cycling and after 5 and 55 cycles are shown in Fig. 7. The enlarged plots at high-intermediate frequency can be seen in Fig. S6.† There are two depressed semicircles instead of one at high-intermediate frequency after the cycling process. These two semicircles can be assigned to the SEI formation which exists after the charge-discharge process and interfacial charge-transfer. The sloping line in the low-frequency region can be assigned to the lithium diffusion impedance.[37] The diameter of the depressed semicircle before cycling is obviously larger than that after cycling, that is because of the non-close contact between the active material and conductive agent which has been verified by a previous report.[38] Accompanying the cycling process, the volume change of matrix Si leads to loss of electrical contact between the active materials and the current

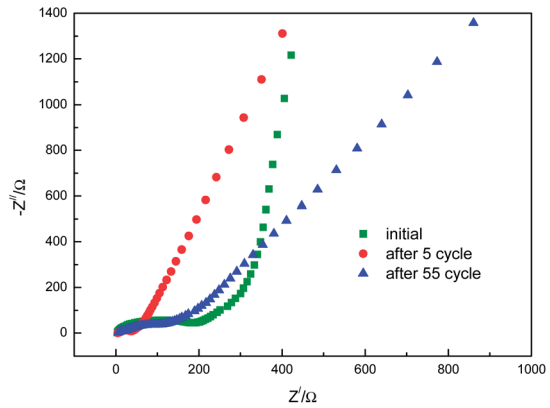

Fig. 7 Nyquist plots for the Si NSs anode before cycling and after 5 and 55 cycles.

collector, and SEI films formed on the fresh surfaces, this resulting in increase of the resistance. What's more, the angle of the low-frequency sloping line shifts to a low angle with increased cycle numbers, implying regression of the lithium diffusion process.[39] However, the angle is also bigger than 45° demonstrating a fast lithium diffusion process in 2D Si NSs anode. As 2D nanostructures, the thin NSs can offer an effective channel, through which the lithium ions and electrons can be transferred fast. The prepared high-yield ultrathin Si NSs show stable lithium storage properties, fast lithium ions transport and the above characteristics make Si NSs a promising candidate for Li-ions batteries' anode material.

Experimental

Synthesis of Si NSs

The as-prepared Si NSs powders were fabricated by a DC arc discharge method under an atmosphere mixture of hydrogen and argon in a volume ratio of 1 : 2. In the experiment, a bulk Si was used as the raw material (anode), while a tungsten rod served as the cathode. As the arc was ignited, DC current was set at 90 A and the voltage was maintained at about 20 V by electrical power supply and by adjusting the space between the two electrodes. The Si NSs powders were deposited on the water-cooled walls of the evaporation chamber and collected after the passivation process.

Characterizations of Si NSs

The Si NSs powders were analyzed by means of X-ray diffraction (XRD, PANalytical Empyrean) using Cu Kα radiation ($\lambda = 1.5416$ Å), Raman microscopy (InVia) with a laser excitation wavelength of 632.8 nm. The structures and morphologies were further characterized by TEM (Tecnai^{2}20 S-TWIN) and AFM (DI-Multimode NS3A-02).

Electrochemical measurements

Electrochemical performances were characterized in CR2025-type half-coin cells. The working electrodes were prepared by mixing active material (Si NSs powders), conductive agent (graphene) and binder agent (Na-Carboxyl Methyl Cellulose, CMC) in a weight ratio of 45 : 45 : 10. The resultant slurry was pasted on a copper foil and dried in an oven at 120 °C for 10 h under vacuum. Then the cells were assembled in an Ar-filled glove box with the contents of moisture and oxygen less than 0.1 ppm. The electrolyte solution was 1 M LiTFSI dissolved in a mixture of ethylene carbonate (EC)/and diethyl carbonate (DEC) (1 : 1, v/v). Li foil was used as the counter electrode and Celgard 2400 as the separator. The discharge/charge cycles of the cells were measured on a LAND CT2001A cell test instrument. Cyclic voltammogram (CVs) measurements of the cells were performed on a CHI660D-1 electrochemical workstation. Electrochemical impedance spectroscopy (EIS) measurements were also conducted on the same electrochemical workstation over a frequency range of 100 kHz to 0.01 Hz.

Conclusions

In summary, ultrathin 2D Si NSs are successfully synthesized by a scalable DC arc-discharge plasma method. The size of the obtained Si NSs is 20 nm in 2D direction and 2.4 nm in thickness which is about 8 atomic layers. A proper ratio of hydrogen and argon is a key role for the 2D growth of Si NSs. The as-achieved Si NSs show stable lithium storage properties and rate performance. EIS shows the lithium ions can be transferred quickly in this kind of materials due to the unique 2D structure.

Acknowledgements

Financial support from the National Basic Research Program of China (grant no. 2011CB936002), the Fundamental Research Funds for Central Universities (2012DUT12RC(3)101), and the National Natural Science Foundation of China (no. 51271044, 11004019 and 51171033).

References

1 X. Han, K. Zheng, Y. Zhang, X. Zhang, Z. Zhang and Z. Wang, *Adv. Mater.*, 2007, **19**, 2112.
2 R. D. Tilley, J. H. Warner, K. Yamamoto, I. Matsui and H. Fujimori, *Chem. Commun.*, 2005, 1833.
3 T. Song, J. Xia, J. H. Lee, D. H. Lee, M. S. Kwon, J. M. Choi, J. Wu, S. K. Doo, H. Chang, W. I. Park, D. S. Zang, H. Kim, Y. Huang, K. C. Hwang, J. A. Rogers and U. Paik, *Nano Lett.*, 2010, **10**, 1710.
4 C. K. Chan, H. Peng, G. Liu, K. Mcilwrath, X. F. Zhang, R. A. Huggins and Y. Cui, *Nat. Nanotechnol.*, 2008, **3**, 31.
5 C. Zhang, A. De Sarkar and R. Q. Zhang, *J. Phys. Chem. C*, 2011, **115**, 23682.
6 H. C. Shin, J. A. Corno, J. L. Gole and M. Liu, *J. Power Sources*, 2005, **139**, 314.
7 C. Yu, X. Li, T. Ma, J. Rong, R. Zhang, J. Shaffer, Y. An, Q. Liu, B. Wei and H. Jiang, *Adv. Energy Mater.*, 2012, **2**, 68.
8 M. J. Sailor and E. C. Wu, *Adv. Funct. Mater.*, 2009, **19**, 3195.
9 T. Hang, H. Nara, T. Yokoshima, T. Momma and T. Osaka, *J. Power Sources*, 2013, **222**, 503.
10 J. Wolfenstine, *J. Power Sources*, 1999, **79**, 111.

11 W. Wang, M. K. Datta and P. N. Kumta, *J. Mater. Chem.*, 2007, **17**, 3229.
12 T. Hasegawa, S. R. Mukai, Y. Shirato and H. Tamon, *Carbon*, 2004, **42**, 2573.
13 M. S. Park, S. Rajendran, Y. M. Kang, K. S. Han, Y. S. Han and J. Y. Lee, *J. Power Sources*, 2006, **158**, 650.
14 C. K. Chan, R. N. Patel, M. J. O'Connell, B. A. Korgel and Y. Cui, *ACS Nano*, 2010, **4**, 1443.
15 R. Teki, M. K. Datta, R. Krishnan, T. C. Parker, T. M. Lu, P. N. Kumta and N. Koratkar, *Small*, 2009, **5**(20), 2236.
16 H. Wu and Y. Cui, *Nano Today*, 2012, **7**, 414.
17 J. Liu and X. W. Liu, *Adv. Mater.*, 2012, **24**, 4097.
18 G. Wang, X. Shen, J. Yao and J. Park, *Carbon*, 2009, **47**, 2049.
19 V. V. Kulish, O. I. Malyi, M. F. Ng, P. Wu and Z. Chen, *RSC Adv.*, 2013, **3**, 4231.
20 H. Okamoto, Y. Sugiyama and H. Nakano, *Chem. - Eur. J.*, 2011, **17**, 9864.
21 A. Kara, H. Enriquez, A. P. Seitsonen, L. C. L. Y. Voon, S. Vizzini, B. Aufray and H. Oughaddoub, *Surf. Sci. Rep.*, 2012, **67**, 1.
22 H. Nakano, T. Mitsuoka, M. Harada, K. Horibuchi, H. Nozaki, N. Takahashi, T. Nonaka, Y. Seno and H. Nakamura, *Angew. Chem.*, 2006, **118**, 6451.
23 U. Kim, I. Kim, Y. Park, K. Y. Lee, S. Y. Yim, J. G. Park, H. G. Ahn, S. H. Park and H. J. Choi, *ACS Nano*, 2011, **5**(3), 2176.
24 Z. Lu, J. Zhu, D. Sim, W. Zhou, W. Shi, H. H. Hng and Q. Yan, *Chem. Mater.*, 2011, **23**, 5293.
25 G. Faraci, S. Gibilisco, P. Russo, A. R. Pennisi and S. L. Rosa, *Phys. Rev. B: Condens. Matter Mater. Phys.*, 2006, **73**, 033307.
26 A. A. Sirenko, J. R. Fox, I. A. Akimov, X. X. Xi, S. Ruvimov and Z. Liliental-Weber, *Solid State Commun.*, 2000, **113**, 553.
27 G. Faraci, S. Gibilisco, A. R. Pennisi and C. Faraci, *J. Appl. Phys.*, 2011, **109**, 074311.
28 C. Meier, S. Luttjohann, V. G. Kravets, H. Nienhaus, A. Lorke and H. Wiggers, *Phys. E.*, 2006, **32**, 155.
29 R. Wang, G. Zhou, Y. Liu, S. Pan, H. Zhang, D. Yu and Z. Zhang, *Phys. Rev. B: Condens. Matter*, 2000, **61**, 16827.
30 C. Li, C. S. Lee, X. Ma, N. Wang, R. Zhang and S. T. Lee, *Adv. Mater.*, 2003, **15**, 607.
31 G. Guo, H. Huang, F. Xue, C. Liu, H. Yu, X. Quan and X. Dong, *Surf. Coat. Technol.*, 2013, **228**, S120.
32 S. D. Beattie, D. Larcher, M. Morcrette, B. Simon and J. M. Tarascon, *J. Electrochem. Soc.*, 2008, **155**, A158.
33 T. Zhang, J. Gao, L. Fu, L. Yang, Y. Wu and H. Wu, *J. Mater. Chem.*, 2007, **17**, 1321.
34 S. Chou, J. Wang, M. Choucair, H. Liu, J. A. Stride and S. Dou, *Electrochem. Commun.*, 2010, **12**, 303.
35 A. Magasinski, P. Dixon, B. Hertzberg, A. Kvit, J. Ayala and G. Yushin, *Nat. Mater.*, 2010, **9**, 353.
36 Z. Lu, J. Zhu, D. Sim, W. Shi, Y. Y. Tay, J. Ma, H. H. Hng and Q. Yan, *Electrochim. Acta*, 2012, **74**, 176.
37 Z. Guo, Z. Zhao, H. Liu and S. Dou, *Carbon*, 2005, **43**, 1392.
38 Y. Kumai, S. Shirai, E. Sudo, J. Seki, H. Okamoto, Y. Sugiyama and H. Nakano, *J. Power Sources*, 2011, **196**, 1503.
39 Y. Peng, Z. Chen, J. Wen, Q. Xiao, D. Weng, S. He, H. Geng and Y. Lu, *Nano Res.*, 2011, **4**(2), 216.